High-pressure synthesis and physical properties of the single-layer nickelate oxychalcogenides $Ba_2NiO_2Cu_2X_2$ (X = S and Se)

Zhen Dong,[1,2,*] Xiao Wang,[2,*] Yingying Cao,[2,*] Wenhui Liu,[2] Yu Liu,[2] Xubin Ye,[3] Guangyang Dai,[2] Guoxiang Guan,[2] Zhiwei Hu,[4] Chang-Yang Kuo,[5,6] Chien-Te Chen,[6] Wenmin Li,[2,†] Yongbing Xue,[1,‡] Youwen Long,[3] Xiancheng Wang,[3,§] and Changqing Jin[3,¶]

[1]*College of Chemical Engineering and Technology, Taiyuan University of Science and Technology, Taiyuan 030024, China*

[2]*Institute of Quantum Materials and Physics, Henan Academy of Sciences, Zhengzhou 450046, China*

[3]*Beijing National Laboratory for Condensed Matter Physics, Institute of Physics, Chinese Academy of Sciences, Beijing 100190, China*

[4]*Max Planck Institute for Chemical Physics of Solids, Nöthnitzer Straße 40, 01187 Dresden, Germany*

[5]*Department of Electrophysics, National Yang Ming Chiao Tung University, Hsinchu 30010, Taiwan*

[6]*National Synchrotron Radiation Research Center (NSRRC), Hsinchu Science Park, Hsinchu 300092, Taiwan*

(Received 14 February 2026; revised 22 April 2026; accepted 29 April 2026; published 29 May 2026)

New single-layer nickelate oxychalcogenides $Ba_2NiO_2Cu_2X_2$ (X = S and Se) were successfully synthesized by using a high-pressure high-temperature method. They crystallize into the tetragonal space group *I*4/*mmm* with alternating NiO_2 square planar and Cu_2Se_2 antifluorite layers along the c direction. High-pressure synchrotron x-ray diffraction manifests that the $Ba_2NiO_2Cu_2Se_2$ can be fairly compressed along the c direction, whereas the ab plane is quite rigid, corresponding to its layered feature. The valence states of Ni^{2+} and Cu^{1+} were validated from both bond valence sums and x-ray absorption spectroscopy. The magnetization of $Ba_2NiO_2Cu_2S_2$ follows the Curie-Weiss law, whereas a spin-glass-like behavior emerges below $T_{sg} = 5$ K. On the other hand, $Ba_2NiO_2Cu_2Se_2$ experiences a low-dimensional antiferromagnetic transition at $T_N = 200$ K. The resistivity of both compounds follows the thermal activation model at elevated temperatures and follows the three-dimensional variable-range hopping model at low temperatures, indicating the semiconducting or insulating nature. DFT+U calculations indicate that weak antiferromagnetic coupling in the NiO_2 layer suppresses the Fermi surface, thereby opening a gap in the electronic structure. The electrical resistance gradually decreases under high pressure, no superconductivity was observed up to 21.4 GPa. This work provides an insight to explore new layered nickelates with emergent physical properties and potential superconductivity.

DOI: 10.1103/49kv-rlm7

I. INTRODUCTION

The layered oxychalcogenide with the chemical formula $(A_{n+1}M_nO_{3n-1})(M'_2X_2)$ ($n = 1, 2, 3, \ldots$; A = Sr, Ba; $M = 3d$ metal; M'= Cu, Ag; X = S, Se) [1–8] has attracted rising interest, on account of its unique structure possessing both the MO_2 square planar layers similar to the CuO_2 layers in cuprate superconductors [9–13] and the M'_2X_2 antifluorite layers similar with the Fe_2As_2 layers in iron-pnictide superconductors [14–18]. The flexibility of accommodating variable elements enables the $(A_{n+1}M_nO_{3n-1})(M'_2X_2)$ system to be a promising candidate for exploring superconductivity and other emergent phenomena. For example, the oxysulfide $Sr_2CuO_2Cu_2S_2$ consists of CuO_2 planes being considered as a candidate of cuprate superconductor [4,19]. The oxyselenide $Sr_2MO_2Cu_2Se_2$ (M = Co, Ni, Zn) has excellent and promising thermoelectric performance [20,21]. The $Sr_2NiO_2Cu_2X_2$ (X = S, Se) experiences a spin transition from high-spin Ni^{2+} in the selenide-rich compounds to low-spin in the sulfide-rich counterpart [22]. There is also an indication that the monovalent copper in the CuSe layer can be applied in the energy field such as an electrocatalyst for water splitting [23].

The recent resurgence of the nickelates due to the observation of superconductivity in the infinite-layer nickelate [24–27] and the Ruddlesden-Popper family under high pressure [28–31] sheds light on the layered oxychalcogenide since it is able to contain NiO_2 layers as well. In particular, $(A_{n+1}Ni_nO_{3n-1})(Cu_2X_2)$ represents a potential system for exploring superconductivity since it has similar bilayer Ni-O structures to $La_3Ni_2O_7$ when $n = 2$, where the outermost apical O is replaced by Se. When $n = 3$, it features a trilayer nickelate structure. Meanwhile, when $n = 1$, it exhibits structural similarities to the intercalated infinite-layer nickelate, where a Cu_2Se_2 antifluorite-type layer is intercalated between Ba_2NiO_2 layers. However, to our knowledge, the reported $(A_{n+1}Ni_nO_{3n-1})(Cu_2X_2)$ system with NiO_2 layers is quite limited with some single-layer nickelate having been reported. The $Sr_2NiO_2Cu_2X_2$ (X = S, Se) is metallic with a ferrimagnetic transition near 70 K [4,22,32]. The $A_2NiO_2Ag_2Se_2$ (A = Sr, Ba) can only be synthesized under high pressure

*These authors contributed equally to this work
†Contact author: wmli@hnas.ac.cn
‡Contact author: tykjdxxyb@163.com
§Contact author: wangxiancheng@iphy.ac.cn
¶Contact author: Jin@iphy.ac.cn

above 5 GPa. It is a narrow-band semiconductor and forms a G-type antiferromagnetic (AFM) order below 130 K [33,34].

Our goal was to synthesize the compound with $n = 2$ or 3 as in the bilayer or trilayer nickelates, which might become a high-T_C superconductor under high pressure. However, only $Ba_2NiO_2Cu_2X_2$ (X = S and Se), which are the compounds with $n = 1$, have been successfully synthesized. The structure of such a single-layered nickelate oxychalcogenide is depicted in Fig. 1(a).

Here, we report the synthesis and detailed characterization of the new single-layer nickelates $Ba_2NiO_2Cu_2X_2$ (X = S and Se). They were synthesized by using a high-pressure technique, which provides an additional degree of freedom to overcome the potential barrier of the chemical reactions, an environment isolated from the air, and prominently reduces the reaction time [35–38]. The $Ba_2NiO_2Cu_2X_2$ (X = S and Se) crystallize into the tetragonal space group *I*4/*mmm* with alternative NiO_2 square planar and Cu_2Se_2 antifluorite layers, and the Ba atoms reside between the layers. High-pressure synchrotron x-ray diffraction shows that the $Ba_2NiO_2Cu_2Se_2$ (BNOCSe) can be fairly compressed along the c direction, whereas the ab plane is quite rigid, corresponding to its layered feature. The valence states of Ni^{2+} and Cu^{1+} were validated from both bond valence sums and x-ray absorption spectroscopy. The magnetization of $Ba_2NiO_2Cu_2S_2$ (BNOCS) follows the Curie-Weiss law, whereas a spin-glass-like behavior emerges below the spin glass transition temperature $T_{sg} = 5$ K. On the other hand, $Ba_2NiO_2Cu_2Se_2$ experiences a low-dimensional antiferromagnetic transition at $T_N = 200$ K. The resistivity of both compounds follows the thermal activation model at elevated temperatures and follows the three-dimensional variable-range hopping model at low temperatures. This indicates their semiconducting or insulating nature. First-principles calculations reveal the interplay of NiO_2 layer and the Cu_2X_2 layer and demonstrate that antiferromagnetic frustration has a pronounced impact on the electronic structure.

II. EXPERIMENTAL

Polycrystalline $Ba_2NiO_2Cu_2S_2$ and $Ba_2NiO_2Cu_2Se_2$ were synthesized using a high-pressure and high-temperature (HPHT) method. Stoichiometric BaS/BaSe, CuO (99.9%), and Ni (99.9%) powders were selected as the starting materials. The BaS/BaSe precursor was prepared by sintering the mixture of Ba (99.9%) and S/Se powders at 650 °C for 3 hours in an argon atmosphere. The starting materials were thoroughly ground in an agate mortar, pressed into a pellet with a diameter of 6 mm and a thickness of ∼2 mm, in a glove box filled with argon gas. After that, the pellet was loaded into a cubic anvil press. The pressure was slowly increased to 5.5 GPa in 30 minutes, after which the temperature was increased in 10 minutes to 1000 °C for BNOCS and 1050 °C for BNOCSe, and maintained for 15 minutes. Then, the temperature was quenched to room temperature in a few seconds, and the pressure was slowly released to ambient pressure in 1 hour.

Powder x-ray diffraction (XRD) was performed using a Rigaku SmartLab diffractometer with Cu-K_α radiation. The Rietveld refinement [39] was conducted using the GSAS software package [40]. The synchrotron XRD (SXRD) measurements were carried out at the BL15U1 beamline of the Shanghai Synchrotron Radiation Facility (SSRF) (λ = 0.62 Å). Diamonds with 300 μm culet and rhenium gaskets were used [41]. The pressures were determined by the ruby fluorescence method. Energy dispersive x-ray analysis (EDX)

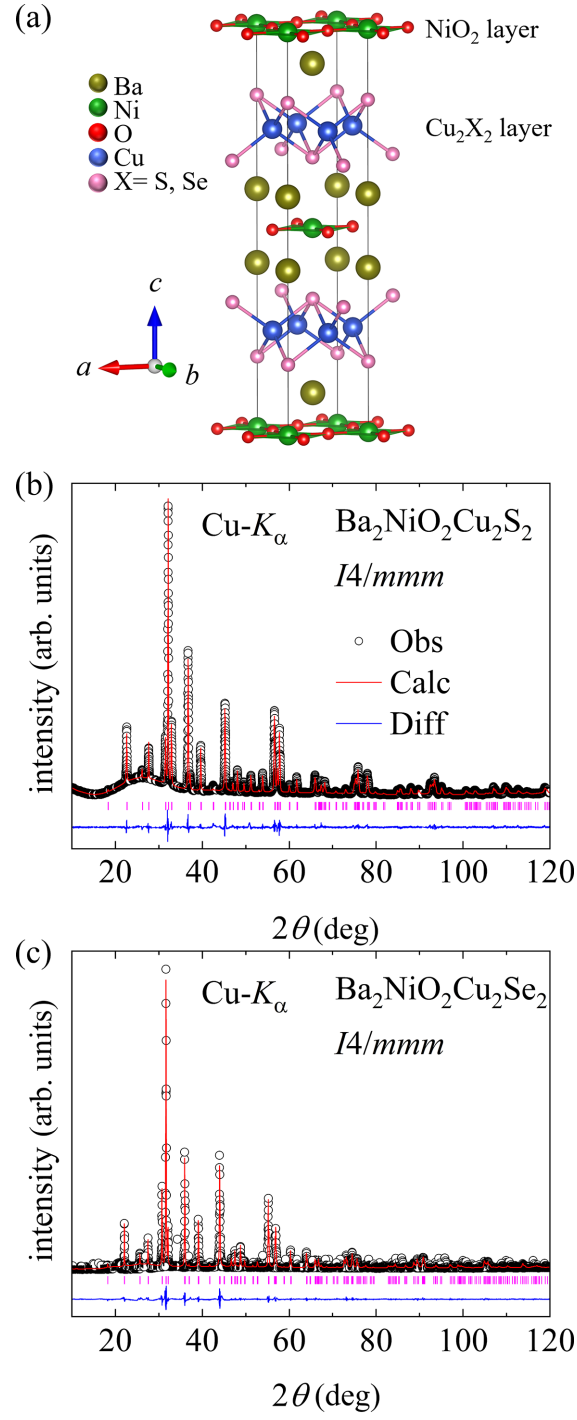

FIG. 1. (a) The crystal structure of $Ba_2NiO_2Cu_2X_2$ (X = S and Se). XRD pattern and Rietveld refinement of (b) BNOCS and (c) BNOCSe. The black circles, red lines, and blue lines indicate the observed, calculated and difference, respectively. The magenta ticks indicate the allowed Bragg reflections for space group *I*4/*mmm*.

with a commercial scanning electron microscope (SEM, Hitachi High-Tech Science Co., Ltd., Tokyo, Japan) was used to analyze the chemical compositions of the powder. The x-ray absorption spectra (XAS) at the Cu-L_3 edge was obtained at the TLS11A beamline of the National Synchrotron Radiation Research Center (NSRRC) using a partial fluorescence yield (PFY) mode with a penetration depth of tens of nanometers [42] to get rid of the surface defects. The Ni-L_3 XAS was obtained at the TLS11A beamline of NSRRC using a total electron yield (TEY) mode with a penetration depth of several nanometers [43] due to remarkable self-absorption of the fluorescence at the Ni-L_3 edge [44]. The sample bulk was cleaved *in situ* under ultrahigh vacuum (10^{-10} mbar) conditions just before the measurement to obtain a fresh surface.

The magnetic measurements were performed using a Quantum Design superconducting quantum interference device magnetometer (MPMS-3). Both zero-field-cooling (ZFC) and field-cooling (FC) modes were adopted under a magnetic field of 1 T. The electrical resistivity was measured using a Quantum Design physical property measurement system (PPMS-DynaCool) with a standard four-probe method. The specific heat was measured using PPMS. The sample was mounted using Apiezon N grease to ensure good thermal contact. The specific heat data were corrected by subtracting the contributions from the sample puck and the grease.

First-principles calculations were performed by using the full-potential linearized augmented plane-wave method as implemented in the WIEN2K package [45]. The experimental crystal structure parameters were adopted. The muffin-tin radii were set to 2.35 a.u. for Ba, 2.35 a.u. for Cu, 2.13 a.u. for S, 2.31 a.u. for Se, 1.74 (1.79) a.u. for O, and 2.02 (2.08) a.u. for Ni in BNOCS (BNOCSe). We used 2940 (2160) k points in the Brillouin zone and set the cutoff of reciprocal vectors so that $R_{\mathrm{MT}}K_{\mathrm{max}} = 8.05$ (8.23) for BNOCS (BNOCSe). The Perdew-Burke-Ernzerhof generalized gradient approximation (GGA-PBE) exchange-correlation functional was employed [46]. In the GGA + U calculations, an empirical effective coulomb interaction of $U_{\mathrm{eff}} = 6$ eV for Ni and 7 eV for Cu was adopted, consistent with commonly used values in Refs. [7,47–48]. Nonmagnetic (NM), ferromagnetic (FM), and antiferromagnetic (AFM) configurations within the NiO_2 layer were examined using spin-polarized calculations.

III. RESULTS AND DISCUSSION

Figures 1(b) and 1(c) display the XRD patterns of BNOCS and BNOCSe, respectively. The sharp and well-resolved diffraction peaks can be well fitted with the *I*4/*mmm* (No. 139) space group, and the refined crystallographic parameters are listed in Table I. The lattice parameters a and c of BNOCSe are larger than those of BNOCS because Se has a larger radius than S. The crystal structure is isostructural with that of $Sr_2NiO_2Cu_2X_2$ (X = S, Se) and $A_2NiO_2Ag_2Se_2$ (A = Sr, Ba) [22,33]. As depicted in Fig. 1, the lattice is constructed with alternating NiO_2 layers (featuring corner-shared NiO_4 square planars) and Cu_2Se_2 antifluorite layers. The Ba atoms are intercalated between the Cu_2X_2 and NiO_2 layers. Compared with the isostructural $Ba_2CuO_2Cu_2Se_2$ with CuO_2 layers [7], the slight expansion of the lattice parameters of BNOCS can be ascribed to the replacement of Cu with Ni in the NiO_2 layers.

TABLE I. Crystallographic parameters of $Ba_2NiO_2Cu_2X_2$ (X = S and Se). The space group is *I*4/*mmm* (No.139), with the Wyckoff positions: Ba (0, 0, z), Ni (0, 0, 0), Cu (0, 0.5, 0.25), O (0, 0.5, 0), and X (0, 0, z). The BVS values (V_i) were calculated using the formula $V_i = \Sigma_j S_{ij}$, where $S_{ij} = \exp[(r_0 - r_{ij})/0.37]$. The values of r_0 are 1.675 Å for Ni^{2+}(−O), 2.04 Å for Ni(–S), 2.14 Å for Ni(–Se), 1.86 Å for Cu(–S), and 2.02 Å for Cu(–Se).

	X = S	X = Se
a (Å)	3.99892(2)	4.11286(2)
c (Å)	19.2739(2)	19.4448(2)
z (Ba)	0.40382(3)	0.40839(5)
z (X)	0.17662(9)	0.17534(8)
U_{iso}(Ba) (100 × Å^2)	0.09(2)	0.11(3)
U_{iso}(Ni) (100 × Å^2)	0.27(7)	0.39(1)
U_{iso}(Cu) (100 × Å^2)	0.36(6)	0.22(7)
U_{iso}(O) (100 × Å^2)	0.61(4)	0.72(4)
U_{iso}(X) (100 × Å^2)	0.28(5)	0.07(3)
R_{wp} (%)	2.87	3.58
R_{p} (%)	1.94	2.41
Ni–O (Å) (×4)	1.9995(1)	2.0564(1)
Ni–X(Å) (×2)	3.4043(2)	3.4093(3)
Cu–X(Å) (×4)	2.4490(13)	2.5173(9)
BVS (Ni)	+1.71	+1.49
BVS (Cu)	+0.81	+1.04

To analyze the element composition of both BNOCS and BNOCSe, we performed the EDX measurement, as depicted in Fig. 2. Given the polycrystalline nature, we also measured the overall composition of $Ba_2NiO_2Cu_2S_2$ and $Ba_2NiO_2Cu_2Se_2$ with surfaces of over 100 μm x100 μm. The compositions from the large surface, $Ba_2Ni_{0.96}O_2Cu_{1.72}S_{1.78}$ and $Ba_2Ni_{0.81}O_2Cu_{2.05}Se_{1.85}$, are close to the nominal $Ba_2NiO_2Cu_2S_2$ and $Ba_2NiO_2Cu_2Se_2$, respectively. The slightly higher Cu content and slightly lower Ni content from EDX suggest that a small amount of Cu may have substituted for Ni. Therefore we rechecked the refinements of the occupancy of Cu and Ni and took into account the scenario of anti-occupation (where Ni occupies the Ni_2Se_2 layers and Cu is situated at the CuO_2 planes). The results indicated that the maximum anti-occupancy ratio of Cu was ∼3.8% in BNOCSe, while the maximum ratio of Ni substituted for Cu in the Cu_2Se_2 layers was ∼1.8%. The identical oxidation state and similar ionic radius of Ni^{2+}(0.69 Å) and Cu^{2+}(0.77 Å) facilitate the feasibility of substitution. In contrast, in $Sr_2NiO_2NiO_2Cu_2S_2$ and $Sr_2NiO_2Cu_2Se_2$ [22], the sites within the oxide layer are exclusively by Ni, which is different from the substitution situation in our samples. Furthermore, the XAS measurements in the subsequent analysis also indicate that Cu substituted for Ni in the NiO_2 layer, but the proportion is extremely low. Considering the small amount of substitution for Ni, we still carry on with further discussions based on the nominal stoichiometry $Ba_2NiO_2Cu_2X_2$, unless specifically stated otherwise.

We performed the bond valence sum (BVS) [49,50] calculations based on the bond lengths, and the results are listed in Table I. The valence states of Ni and Cu are close to +2 and

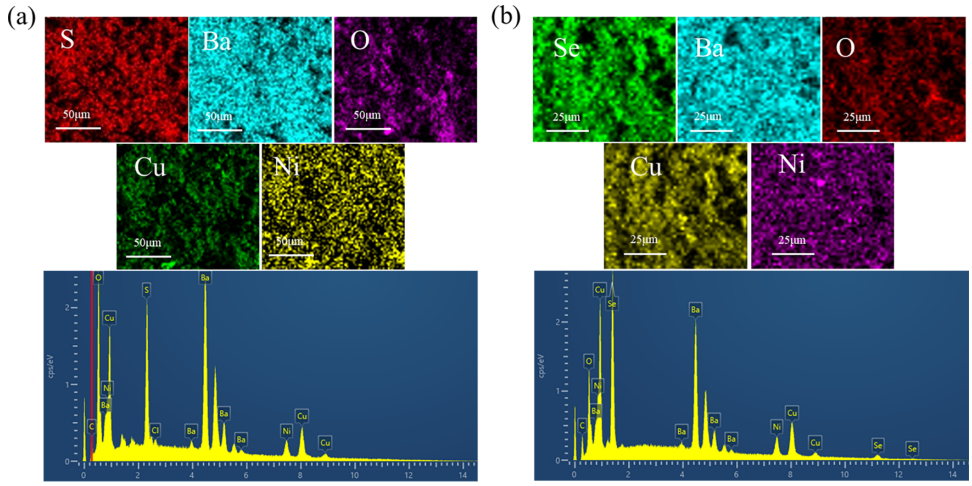

FIG. 2. EDX spectra of (a) BNOCS and (b) BNOCSe and the elemental map of Ba, S/Se, O, Cu, and Ni.

+1, respectively, in agreement with the charge conservation when considering that the O and Se have valence states of −2. The valence state of Ni is slightly underestimated by BVS due to the NiO_4 square planar coordination.

In order to directly determine the valence states of Ni and Cu in BNOCS and BNOCSe, we performed XAS measurements using a synchrotron x-ray beam. As is widely recognized, the element selective XAS at the transition metal L_3 edges is highly sensitive to the valence state. Specifically, in an open d-shell system, an increase of one unit in valence state typically induces a 1–2 eV shift in the white line of the spectrum toward higher photon energy, alongside notable changes in peak features [51–58].

The Cu-L_3 XAS of BNOCS and BNOCSe, as well as CuO as a Cu^{2+} reference and Cu_2O as Cu^{1+} reference [55,56], are illustrated in Fig. 3(a). The strong peak in CuO represents a transition from $2p$ core hole to $3d$ state with $3d^9$ ground state. One can observe a weak feature at the L_3 of Cu_2O, which is located at higher energy (933.6 eV) than that of the Cu^{2+} (931.3 eV). This is assigned to the $4s$-related states since the $3d$ states are fully occupied for the $3d^{10}$ electronic configuration for Cu^{1+} [57,58]. For BNOCS and BNOCSe, there is no intensity related to transition to localized $3d$ state indicating a Cu^{1+} ground state. The weak and broad spectral features localize at higher energy than that in Cu_2O reflecting more delocalized unoccupied band structure due to Cu-Se covalency. For comparison, the Cu-L_3 XAS of $Ba_2CuO_2Cu_2Se_2$ [7] was depicted in Fig. 3(a) (magenta line). A strong contribution of Cu^{2+} feature can be observed corresponding to the CuO_2 layer. The XAS spectra of both BNOCS and BNOCSe show a relatively weak and broad bump near 931.3 eV, which should be attributed to the Cu^{2+}. Considering the suppression of spectral weight for Cu^{1+} with a filled shell in XAS, the Cu^{2+} content is extremely low, which is consistent with the XRD refinements. Thus, XAS spectra of BNOCS and BNOCSe further manifest that the Cu^{1+} are almost fully accommodated in the Cu_2Se_2 antifluorite layer. The Ni-L_3 XAS of BNOCS, BNOCSe, and a reference NiO are displayed in Fig. 3(b). The energy position (851.2 eV) of the L_3 peak of BNOCS and BNOCSe is located at the identical energy position of that of NiO, and the line shape resembles that of NiO, indicating a *high-spin* Ni^{2+} state in both BNOCS and BNOCSe.

Figure 4(a) displays the temperature-dependent magnetic susceptibility (χ) of BNOCS. A spin-glass-like behavior can be observed at $T_{sg} = 5$ K as depicted in the inset of Fig. 4(a), indicating the magnetic frustration, which could be the result

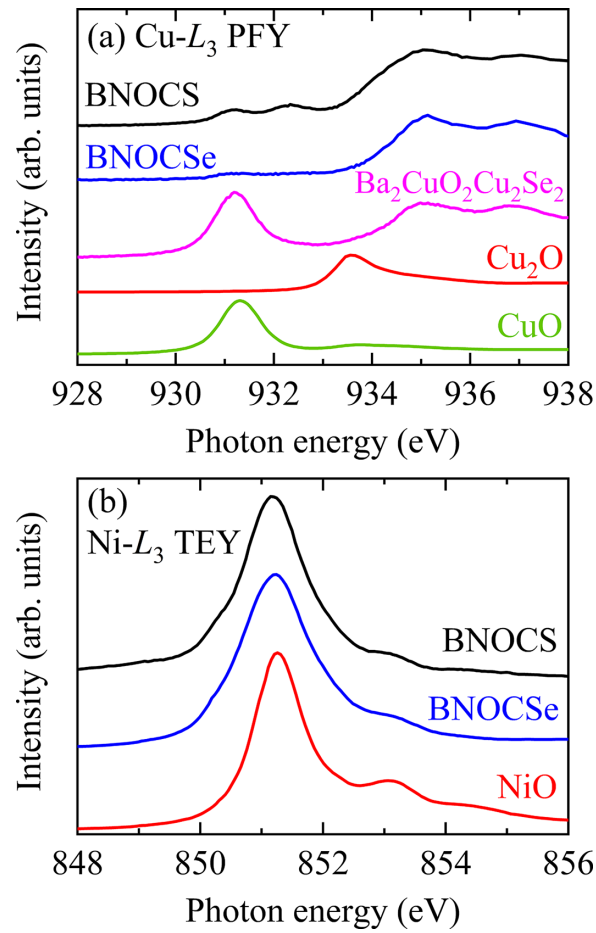

FIG. 3. XAS at the (a) Cu-L_3 and (b) Ni-L_3 of BNOCS and BNOCSe. The XAS of some references is displayed.

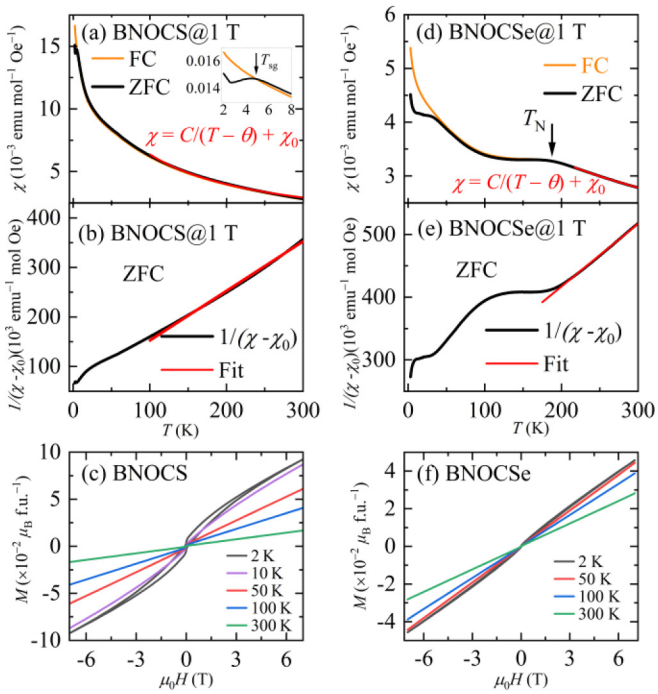

FIG. 4. Temperature-dependent magnetic susceptibility of (a) BNOCS and (d) BNOCSe. Both ZFC (black line) and FC (orange line) modes are shown. The reverse susceptibility and the fit (red line) of (b) BNOCS and (e) BNOCSe using the Curie-Weiss law. The Curie-Weiss fitting was shown in red line. Field-dependent magnetization of (c) BNOCS and (f) BNOCSe at selected temperatures.

of the geometric frustration of the AFM coupling between the nearest and second nearest Ni cations [5,59]. To quantitatively evaluate the magnetic coupling, i.e., the Weiss temperature θ, we performed Curie-Weiss fitting at a temperature range of 100–300 K using the equation

$$\chi = C/(T-\theta)+\chi_0. \quad (1)$$

Given that the magnetic susceptibility of BNOCS is very small, the residual magnetic susceptibility χ_0 should be taken into consideration. Figure 4(b) displays the inverse susceptibility $1/(\chi-\chi_0)$ versus temperature. It is obvious that the curve displays a straight line in the high temperature range of 150–300 K with the obtained $\chi_0 = 2.54\times10^{-5}$ emu/mol. The positive χ_0 usually comes from the Van Vleck paramagnetism in an insulator [5]. From the discussion above, we have determined the high-spin Ni^{2+} and nonmagnetic Cu^{1+}, leading to an effective magnetic moment of $\mu_{\text{eff}} = 2.83\,\mu_B$/f.u. It is reasonable to set the Curie constant C= 1.00 ($\mu_{\text{eff}} = \sqrt{8C}$). The obtained $\theta = -42$ K corresponds to a weak AFM magnetic coupling in BNOCS. Figure 4(b) depictes the field-dependent magnetization of BNOCS. At temperatures above T_{sg}, linear $M(H)$ curves are found, in correspondence to the paramagnetic states. At 2 K, a coercive field emerges, corresponding to the spin-glass state.

The spin-glass-like behavior of BNOCS was further validated by the ac magnetic susceptibility measurements. As displayed in Fig. 5, the $M'(T)$ curves of different frequencies gradually separate below 100 K, and an anomaly occurs at $T_{sg} = 5$ K. The M' maximum gradually shifts to higher

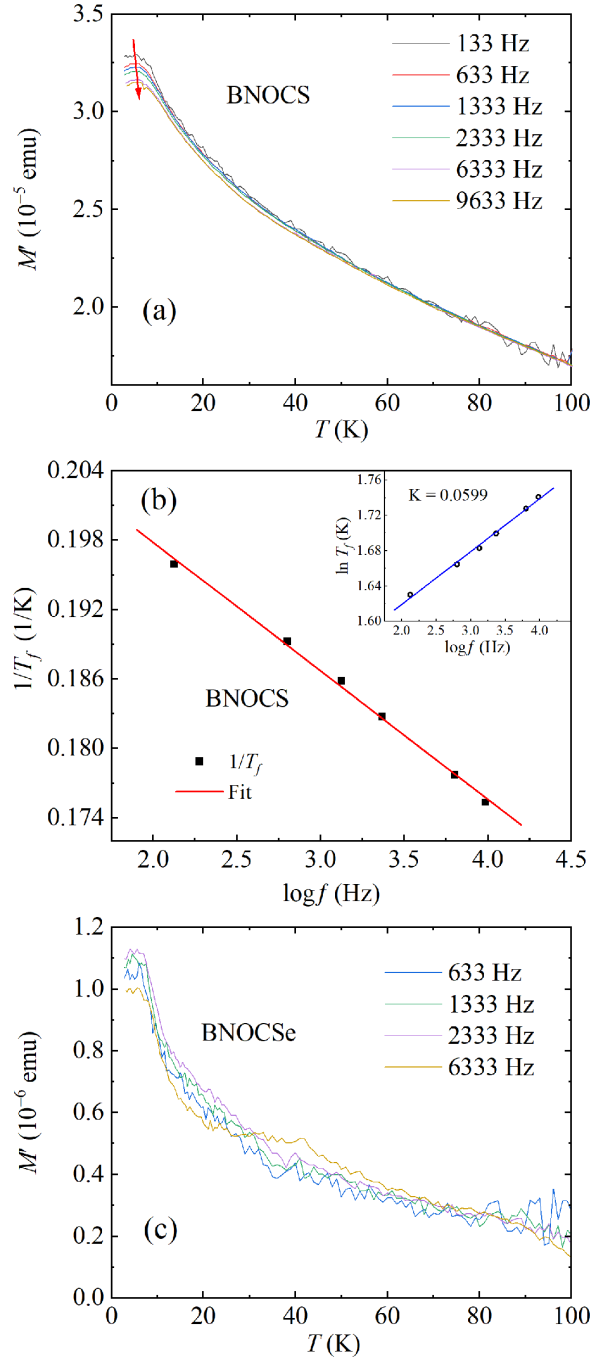

FIG. 5. The real part of the ac magnetization of (a) BNOCS and (c) BNOCSe at selected frequencies. A significantly weaker response compared to BNOCS, with values reduced by more than one order of magnitude. (b) Frequency-dependent analysis of the freezing temperature for BNOCS: main panel shows the reciprocal freezing temperature $1/T_f$ vs the $\log_{10} f$, with a linear fit to the experimental data. The inset illustrates the $\ln T_f$ vs $\log_{10} f$ with a blue fitting line.

temperature, and its value monotonously decreases with frequency increasing, indicating a freezing process of the magnetic moment. The separation between the ZFC and FC curves can be the result of the presence of short-range spin clusters.

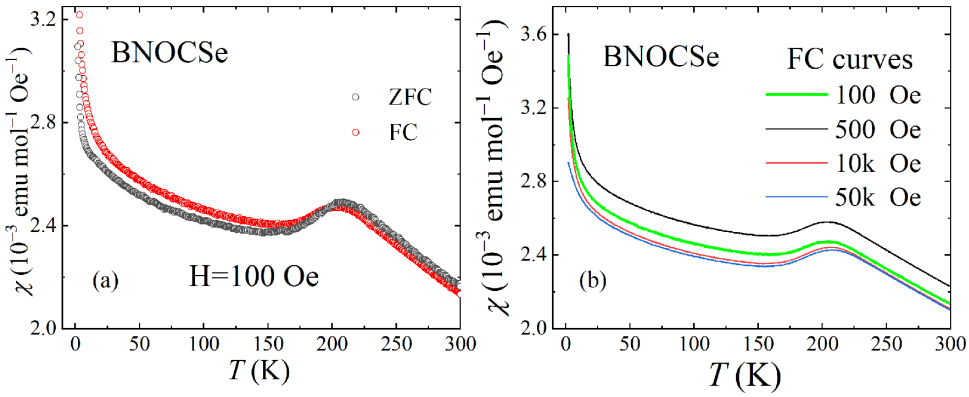

FIG. 6. (a) Temperature dependence of the magnetic susceptibility $\chi = M/H$ of BNOCSe under an applied magnetic field of 100 Oe. (b) FC curves measured at various fields between 100 and 50 kOe, as indicated.

To elucidate the spin glass dynamics, we analyze the frequency dependence of the freezing temperature by plotting the reciprocal freezing temperature $1/T_f$ versus $\log_{10} f$, as shown in Fig. 5(b). The experimental data exhibit excellent agreement with a linear fit, confirming the power-law scaling behavior predicted by the dynamic scaling theory [60]. The parameter $K = \Delta T_f/(T_f \Delta \log_{10} f)$ is used to describe the frequency dependence, as shown in the inset. The obtained $K = 0.06$ for $Ba_2NiO_2Cu_2S_2$ falls in the expected range of values (0.005–0.08) for a typical spin glass system [60–63].

Figure 4(d) displays the temperature-dependent magnetic susceptibility (χ) of BNOCSe. A bump near $T_N = 200$ K can be observed for both ZFC and FC curves, which is also observed in the measurements under varying applied fields (Fig. 6). This feature is reminiscent of a low-dimensional antiferromagnetic (AFM) transition [64,65]. Given that the Cu^{1+} ($3d^{10}$) is nonmagnetic, the transition can be ascribed to the Ni forming an AFM structure inside the NiO_2 layer. To clarify the AFM state of BNOCSe, we also performed the Curie-Weiss fitting using Eq. (1) with $C = 1$ in the temperature range of 220–300 K as shown in Fig. 4(e). The obtained Weiss temperature $\theta = -213$ K (with $\chi_0 = 8.34 \times 10^{-4}$) is obviously lower than that of BNOCS, indicating a more robust AFM coupling in BNOCSe. The χ_0 is much larger than the value in BNOCS. It is an order of magnitude larger than the estimated value coming from the Van Vleck paramagnetism and is hence unphysically large. The anomalously large behavior was also observed in $Sr_2Mn_2CuAs_2O_2$ [5]. In the case of $Sr_2Mn_2CuAs_2O_2$, a ferrimagnetic model was introduced to account for the strong positive curvature in $\chi^{-1}(T)$, which was corroborated by neutron diffraction experiments [5]. This implies that more complex magnetic interactions may potentially exist in BNOCSe, and simple high-spin and low-spin models for Ni^{2+} may not be entirely appropriate in these compounds [22]. With further cooling to about 50 K, the ZFC and FC curves start to separate from each other, a behavior similar to that observed at 5 K in BNOCS. In order to characterize the anomaly, ac magnetic susceptibility of BNOCSe was measured as shown in Fig. 5(c). A significantly weaker response was obtained compared to BNOCS, with values reduced by more than one order of magnitude. A weak anomaly is only observed upon cooling down to ~5.5 K. This implies the potential existence of short-range correlations or dynamic processes arising from domain wall motion, which may also account for the ZFC-FC curves splitting at low temperatures. Consequently, as shown in Fig. 4(f) the field-dependent magnetization of BNOCSe, a linear $M(H)$ behavior was observed over the whole measured temperature range of 2–300 K, corresponding to the paramagnetic state above T_N and the AFM state below T_N. It is worth noting that we also performed the Curie-Weiss fitting using the formula $\chi = C/(T - \theta)$ without fixing $C = 1$. The results indicate the values of $C = 1.67$, $\mu_{eff} = 3.66\,\mu_B$, $\theta = -128$ K for BNCOS and $C = 1.65$, $\mu_{eff} = 3.63\,\mu_B$, $\theta = -347$ K for BNOCSe, respectively. Notably, the obtained μ_{eff} is really large, implying that the NiO_2 layers would need to adopt an extremely high spin state of $S \sim 3/2$, which is clearly unreasonable.

Square-planar coordinated Ni^{2+} ions typically adopt a low-spin ($S = 0$) configuration due to strong crystal field splitting [33], as exemplified by the case of $Sr_2NiO_2Cu_2S_2$ [4,22,32]. In BNOCSe and BNOCS, the high-spin state of Ni^{2+} likely originates from elongated Ni–O bond lengths, analogous to the mechanism observed in $Sr_2NiO_2Cu_2Se_2$, $Sr_2NiO_2Ag_2Se_2$, and $Ba_2NiO_2Ag_2Se_2$ [22,33]. This lattice expansion reduces the crystal field splitting energy as discussed in Ref. [33], thereby stabilizing the high-spin configuration of Ni^{2+}. Interestingly, the bond length in $Ba_2NiO_2Cu_2S_2$ lies at the boundary between these spin states as shown in Table II. In a mixed spin state (or so called intermediate spin state), electrons would transfer from the high-energy $d_{x^2-y^2}$ orbital to the low-energy d_{z^2} orbital, which effectively hole-dopes the $d_{x^2-y^2}$ orbital while electron-doping the d_{z^2} orbital. Super-

TABLE II. Comparison of Ni-O bond length and spin state for $A_2NiO_2M_2X_2$ (A = Sr, Ba; M = Cu, Ag; X = S, Se).

Compounds	Ni-O bond length (Å)	Spin state
$Sr_2NiO_2Cu_2S_2$ [4]	1.962	Low spin
$Ba_2NiO_2Cu_2S_2$	1.999	High spin
$Sr_2NiO_2Cu_2Se_2$ [22]	2.013	High spin
$Sr_2NiO_2Ag_2Se_2$ [32]	2.051	High spin
$Ba_2NiO_2Cu_2Se_2$	2.056	High spin
$Ba_2NiO_2Ag_2Se_2$ [32]	2.128	High spin

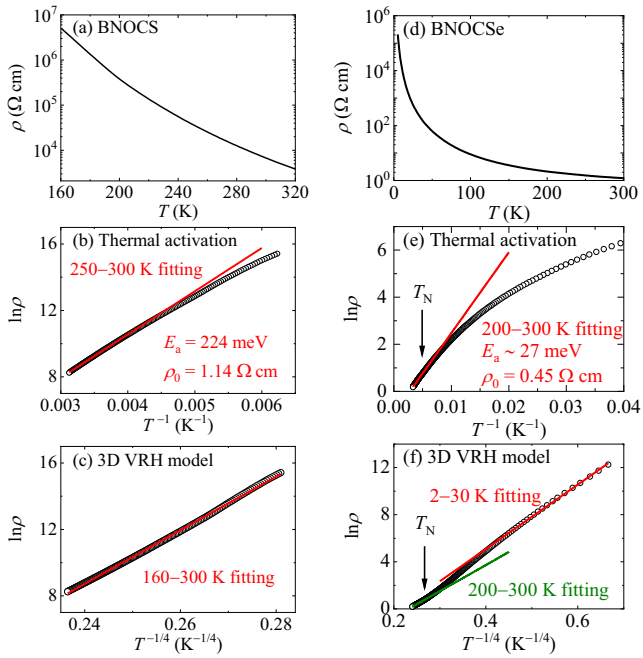

FIG. 7. (a) Temperature dependence of resistivity of BNOCS. (b) The $\ln\rho$-$1/T$ plot of the experimental data (black circles) and the fitting result (red line) of the thermal activation model. (c) The $\ln\rho$-$1/T^4$ plot of the experimental data (black circles) and the fitting result (red line) of the 3D VRH model. (d) Temperature dependence of resistivity of BNOCSe. (e) The $\ln\rho$-$1/T$ plot of the experimental data (black circles) and the fitting result (red line) of the thermal activation model. (f) The $\ln\rho$-$1/T^4$ plot of the experimental data (black circles) and the fitting result (red and green lines) of the 3D VRH model.

conductivity is expected in such a scenario, as observed in heavily hole-doped Ba_2CuO_{4-y} with compressed CuO_6 octahedra, where the d_{z^2} orbital is lifted to the Fermi surface and superconductivity arises from doping of a two-orbital Mott insulator [66,67].

Figure 7(a) depicts the temperature-dependent resistivity of BNOCS. It increases exponentially with cooling and exceeded the measuring range below 160 K, indicating a semiconductive or insulative behavior. In order to verify this, as shown in Fig. 7(b), we plotted the $\ln\rho$-$1/T$ plot and it can be well fitted in the elevated temperature range of 250–300 K using a thermal activation model

$$\ln\rho = E_a/k_B T + \ln\rho_0, \tag{2}$$

where k_B is the Boltzmann constant, ρ_0 is the residual resistance, and E_a is the activation energy. The energy gap is obtained to be $E_k = 2\ E_a = 0.448$ eV and the residual resistivity is $\rho_0 = 0.37\ \Omega$ cm. On the other hand, as shown in Fig. 7(c), a linear $\ln\rho$-$1/T^4$ plot is observed for the whole measured temperature range, indicating that the electron transport of BNOCS follows a three-dimensional (3D) varial-range hopping (VRH) mechanism with the equation

$$\ln\rho = (T_0/T)^{1/4} + \ln\rho_0. \tag{3}$$

Thus the BNOCS is more close to an insulator.

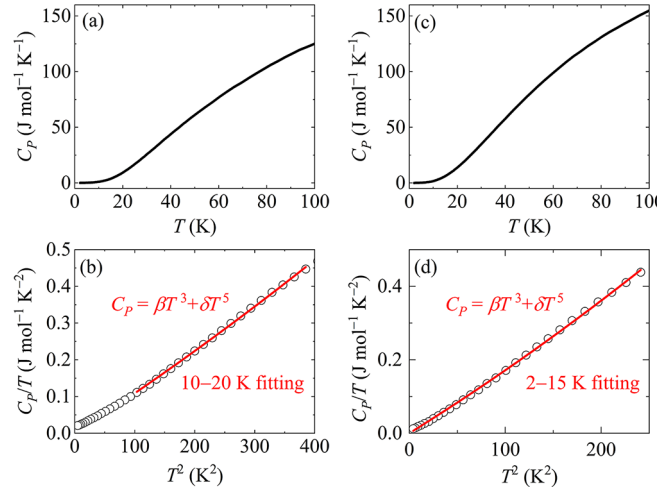

FIG. 8. Temperature dependence of heat capacity of (a) BNOCS and (c) BNOCSe. The C_P/T-T^2 plot at (b) 2–20 K of BNOCS and (d) 2–15 K of BNOCSe. The experimental data and the fitting result are displayed in black circles and the red line, respectively.

Figure 7(d) depicts the temperature-dependent resistivity of BNOCSe. Different from its sulfur counterpart, the resistivity of the selenide sample is quite small ($\sim$1 Ω cm) at room temperature, whereas it increases exponentially with cooling, indicating a semiconductive behavior. As shown in Fig. 7(e), we fitted the $\ln\rho$-$1/T$ plot at 200–300 K using a thermal activation model [Eq. (2)]. The energy gap is obtained to be $E_k = 2$ and$E_a = 54$ meV, and the residual resistivity is $\rho_0 = 0.45\ \Omega$ cm. Figure 7(f) depicts the $\ln\rho$-$1/T^4$ plot of BNOCSe. Different from the sulfur counterpart [Fig. 7(c)], two linear regions were observed at temperatures below and above T_N, respectively. Thus the BNOCSe is closer to a semiconductor at elevated temperatures and an insulator at low temperatures. As a comparison, most materials within the same series exhibit insulating properties, such as $Sr_2NiO_2Cu_2S_2$, $Sr_2NiO_2Ag_2Se_2$, and $Ba_2NiO_2Ag_2Se_2$. Only $Sr_2NiO_2Cu_2Se_2$ displays metallic behavior [22,33].

Figure 8(a) displays the temperature-dependent heat capacity of BNOCS. Its value gradually approaches the Dulong-Petit limit $3NR = 224$ J mol^{-1} K^{-1}, where $N = 9$ is the number of atoms per chemical formula and $R = 8.314$ J mol^{-1} K^{-1} is the ideal gas constant. To determine the components of the heat capacity, we plotted the C_P/T-T^2 at 2–20 K, as displayed in Fig. 8(b). Considering the spin-glass-like transition at $T_{sg} = 5$ K, we fitted the experimental data at 10–20 K considering only the phonons using the formula

$$C_P = \beta T^3 + \delta T^5. \tag{4}$$

The fitted parameters are $\beta = 1.06$ mJ mol^{-1} K^{-4} and $\delta = 3.00 \times 10^{-4}$ mJ mol^{-1} K^{-6}.The Debye temperature of BNOCS is calculated to be $\Theta_D = (12N\pi^4R/5\beta)^{1/3} = 255$ K, which is comparable to that of the isostructural oxypnictides $Sr_2MO_2M'_2As_2$ (M = Mn, Cu; M'= Mn, Zn) [5].

Figure 8(c) displays the temperature-dependent heat capacity of BNOCSe, and Fig. 8(d) displays the C_P/T-T^2 plot at 2–15 K. One can observe a concave C_P/T-T^2 curve with a zero intercept on the vertical axis, indicating that

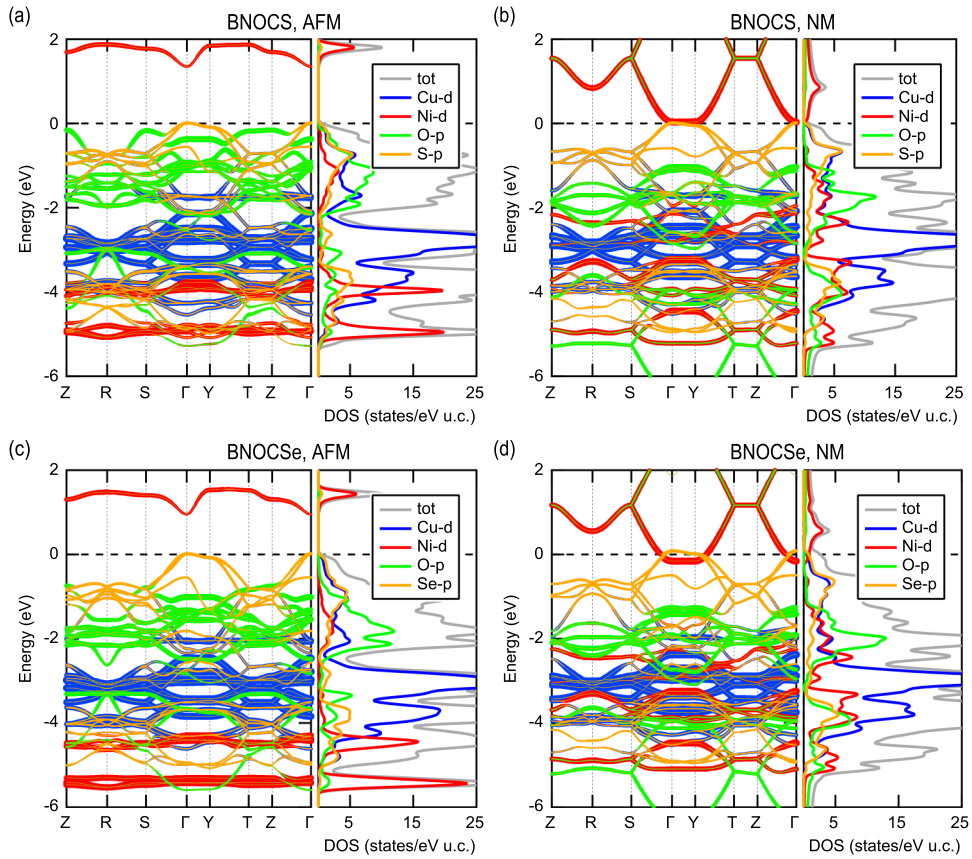

FIG. 9. Electronic band structure and densities of states obtained from first-principles calculations for (a) the AFM state of BNOCS, (b) the NM state of BNOCS, (c) the AFM state of BNOCSe, and (d) the NM state of BNOCSe. The orbital-projected contributions from Cu d, Ni d, O p, and Se p states are shown in blue, red, green and orange, respectively.

only the phonons contribute to the heat capacity. This behavior is in accordance with the fact that BNOCSe is insulating at low temperatures. The C_P/T-T^2 curve can be well fitted using Eq. (4) with $\beta = 1.62\ \mathrm{mJ\,mol^{-1}\,K^{-4}}$ and $\delta = 9.18 \times 10^{-4}\ \mathrm{mJ\,mol^{-1}\,K^{-6}}$, with the Debye temperature of 221 K.

First-principles calculations were carried out to investigate the magnetic and electronic properties of BNOCS and BNOCSe, considering different magnetic configurations and the strong on-site Coulomb interactions of the Cu 3d and Ni 3d electrons. Among the considered magnetic states, the AFM configuration yields the lowest total energy for both BNOCS and BNOCSe, although the energy difference is small. The band structures and the partial density of states for both the NM and AFM states are shown in Fig. 9. The spin magnetic moment inside the muffin-tin spheres are approximately 1.7 μ_B for Ni and nearly zero for Cu, indicating a high-spin $3d^8$ configuration of Ni^{2+} and nonmagnetic Cu^{1+}, consistent with experiment. The NM states are gapless [Figs. 9(b) and 9(d)], which is inconsistent with the experimentally observed semiconducting/insulating behavior. In contrast, the AFM state opens a band gap of ∼1.37 eV (∼0.98 eV) for BNOCS (BNOCSe) [Figs. 9(a) and 9(c)], highlighting the significant influence of AFM exchange on the electronic structure. The valence-band maximum is dominated by S (Se) 4p orbitals, whereas the conduction-band minimum primarily originates from the Ni 3d upper Hubbard band. In the NM state, these bands cross near Γ, suggesting substantial charge transfer from the Cu_2S_2 (Cu_2Se_2) layer to the NiO_2 layer. This crossing is removed by the AFM splitting, indicating that the AFM correlations suppress the effective interlayer charge transfer.

The smaller experimental transport gap may be attributed to 2D AFM fluctuations in the NiO_2 layer, which can partially gap the Fermi-level states in a manner analogous to cuprates, but with a weaker effect due to the relatively small nearest-neighbor Ni-Ni exchange coupling J_{AFM} (62 meV for BNOCS and 5.5 meV for BNOCSe). This interpretation is consistent with the negative Weiss temperature of BNOCSe obtained from Curie-Weiss fitting of magnetic susceptibility, indicating predominantly AFM interactions with weak frustration. In addition, short-circuit effects induced by defects, including grain boundaries, oxygen deficiency, and antisite occupancy, may also contribute to the phenomenon that the fitting values of the energy gap from the $R(T)$ measurements is smaller than the theoretical values. The calculated gap is larger in BNOCS than in BNOCSe, consistent with resistivity measurements. This trend can be attributed to the deeper S 3p levels compared with Se 4p levels, which reduces charge transfer in BNOCS. Our calculations further suggest a stronger AFM coupling within the NiO_2 layer in BNOCS than in BNOCSe, which can be linked to the shorter Ni-O bond length associated with the smaller ionic radius

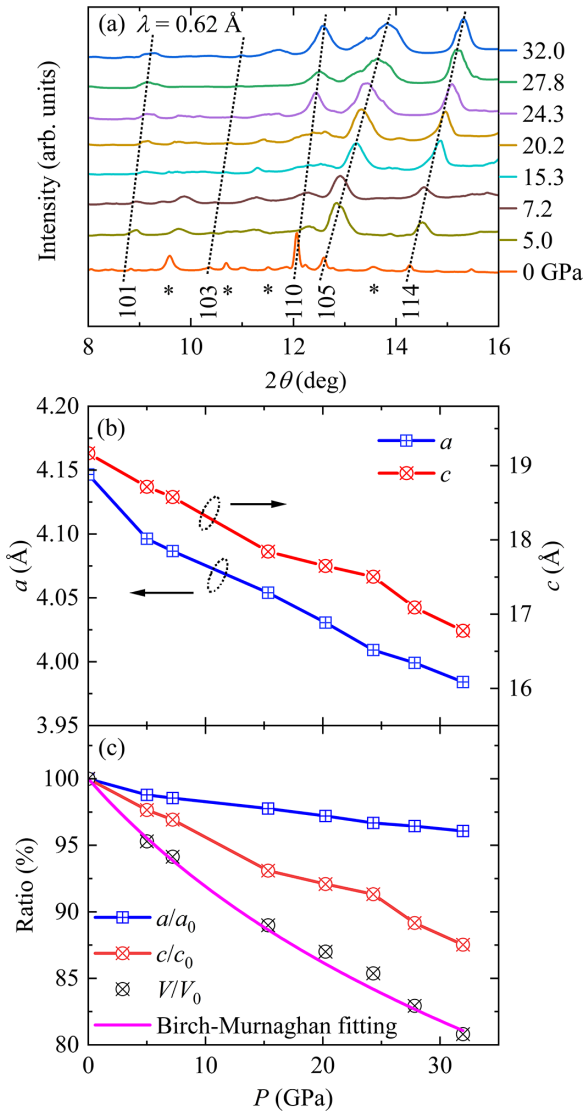

FIG. 10. (a) SXRD pattern of BNOCSe under selected pressures. The stars indicate the diffraction peaks from the background signal and a tiny number of impurities. [(b) and (c)] Variation of lattice parameters as a function of pressure. The magenta line is the fitting by using the Birch-Murnaghan equation.

of S. This trend differs from the experimental observations, which suggests more robust AFM order in BNOCSe. This discrepancy may indicate the presence of additional magnetic interactions, such as next-nearest-neighbor Ni-Ni exchange or interlayer coupling, which are not fully captured in the present approach and warrant further investigation in this exotic family.

We further investigated the structure evolution of BNOCSe under pressure. As shown in Fig. 10(a), with increasing pressure, all the diffraction peaks gradually broaden and shift to higher 2θ angle, indicating that the lattice was compressed under pressure. The lattice parameters a, b and volume as a function of applied pressure are displayed in Figs. 10(a) and 10(b). Under the highest pressure of ~32 GPa we measured, the a lattice experiences a slight reduction about 5% compared with which under ambient pressure, whereas the c

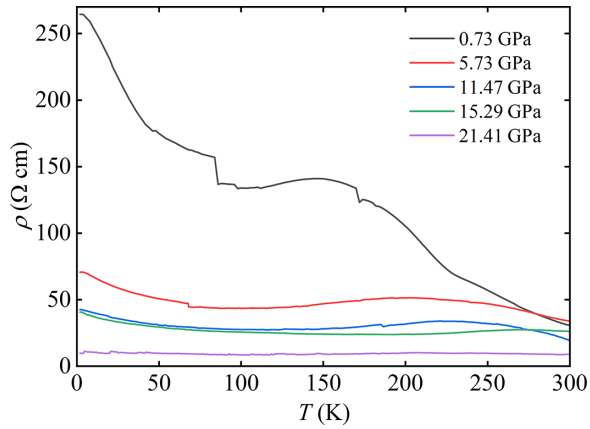

FIG. 11. Pressure evolution of resistance-temperature curves in BNOCSe.

lattice shrinks 17%, in agreement with the layered structure with moderate interlayer stacking. The experimental pressure-volume data are fitted using a third-order Birch-Murnaghan equation of state [68]:

$$P = \frac{3}{2}B_0\left[\left(\frac{V}{V_0}\right)^{-\frac{7}{3}} - \left(\frac{V}{V_0}\right)^{-\frac{5}{3}}\right] \times \left\{1 + \frac{3}{4}(B_0^{'} - 4) \times \left[\left(\frac{V}{V_0}\right)^{-\frac{2}{3}} - 1\right]\right\}, \quad (5)$$

where the bulk modulus $B_0 = 100.04$ GPa and the zero-pressure equilibrium volume $V_0 = 330.85$ Å^3 with constant bulk modulus in the first derivative ($B_0^{'} = 4$). For comparison, the bulk modulus values for steel and diamond are ~160 and ~600 GPa, respectively.

Subsequently, we investigate the transport properties of BNOCSe under pressure. The high-pressure transport measurements were performed up to 21.4 GPa. As shown in Fig. 11, the resistance decreases monotonically under compression, consistently exhibiting semiconductor behavior across the entire pressure range. The poor quality of the resistivity data may be related to the polycrystalline nature of the sample. Grain boundaries and intergranular irregularities can introduce additional scattering and contact resistance, resulting in noisier measurements. In addition, pressure inhomogeneity arising from a pressure gradient within the cell may further deteriorate the data quality. A broad bump can be observed in different pressure curves within the temperature range of 150–250 K, corresponding to the long-range antiferromagnetic transition of BNOCSe. Due to the issue of data quality, we have not provided the exact evolution of T_N with pressures. No superconductivity signal was observed. We suppose that elevating the doping level of Ni to a $Ni^{+2.5}$ valence state, coupled with the suppression of magnetic ordering by applying pressure, could offer an opportunity for superconductivity. Further in-depth research will be carried out after single crystals are grown.

IV. CONCLUSION

In summary, new single-layer nickelates $Ba_2NiO_2Cu_2X_2$ (X = S and Se) were successfully synthesized under high-pressure and high-temperature conditions. $Ba_2NiO_2Cu_2S_2$ demonstrates undergoes a spin-glass-like transition emerges below $T_{sg} = 5$ K, while $Ba_2NiO_2Cu_2Se_2$ experiences a low-dimensional antiferromagnetic transition at $T_N = 200$ K. Both $Ba_2NiO_2Cu_2S_2$ and $Ba_2NiO_2Cu_2Se_2$ adopt the high-spin state of Ni^{2+} likely originating from elongated Ni–O bond lengths, analogous to the mechanism observed in $Sr_2NiO_2Ag_2Se_2$ and $Ba_2NiO_2Ag_2Se_2$. Interestingly, the bond length in $Ba_2NiO_2Cu_2S_2$ lies at the boundary between the high spin and low spin states, which offers additional evidence and provides a clearer demarcation regarding the modulation of Ni^{2+} through the crystal field splitting in square-planar coordinated nickel oxides. The resistivity of both compounds show the semiconducting or insulating nature following the thermal activation model at elevated temperatures and the three-dimensional variable-range hopping model at low temperatures. The first-principles calculations suggest that AFM coupling between nearest-neighbor Ni^{2+} ions drives the gap opening in both $Ba_2NiO_2Cu_2S_2$ and $Ba_2NiO_2Cu_2Se_2$, analogous to the behavior observed in cuprates. The structure of $Ba_2NiO_2Cu_2Se_2$ remains stable under high pressure while the electrical resistance gradually diminishes up to 21.4 GPa. Although our efforts to achieve superconductors have not been successful so far, this work still presents a promising avenue for the exploration of novel layered nickelates and further attempts to explore superconductivity.

ACKNOWLEDGMENTS

This research was funded by the Joint Fund of Henan Province Science and Technology R&D Program (Project No. 245200810084), the High-Level Talent Research Start-Up Project Funding of Henan Academy of Sciences (Projects No. 241827046, No. 242027151, No. 20251827005, and No. 20251827011), the Fundamental Research Fund of Henan Academy of Sciences (Projects No. 240627005 and No. 20260627001), the National Natural Science Foundation of China (Grants No. 12304159 and No. 12474097), the National Key Research and Development Program of China (2023YFA1406001 and 2024YFA1408000); the Beijing National Laboratory for Condensed Matter Physics (Project No. 2023BNLCMPKF006), and the Innovation Program for Quantum Science and Technology (Grant No. 2021ZD0302800). The authors acknowledge the support from the Max Planck-POSTECH-Hsinchu Center for Complex Phase Materials. We thank the Shanghai Synchrotron Radiation Facility of Experiment Assist System [69] for the assistance on the BL15U1, BL17UM and BL14B1 beamlines.

DATA AVAILABILITY

The data that support the findings of this article are not publicly available upon publication because it is not technically feasible and/or the cost of preparing, depositing, and hosting the data would be prohibitive within the terms of this research project. The data are available from the authors upon reasonable request.

[1] X. Zhou, V. S. C. Kolluru, W. Xu, L. Wang, T. Chang, Y.-S. Chen, L. Yu, J. Wen, M. K. Y. Chan, D. Y. Chung, and M. G. Kanatzidis, Discovery of chalcogenides structures and compositions using mixed fluxes, Nature (London) **612**, 72 (2022).

[2] E. Brechtel, G. Cordier, and H. Schäfer, Über oxidpnictide: Zur kenntnis von $A_2Mn_3B_2O_2$ mit A = Sr, Ba und B = As, Sb, Bi / On oxidpnictides: Preparation and crystal structure of $A_2Mn_3B_2O_2$ with A = Sr, Ba and B = As, Sb, Bi, Z. Naturforsch. B **34**, 777 (1979).

[3] W. J. Zhu, P. H. Hor, A. J. Jacobson, G. Crisci, T. A. Albright, S. H. Wang, and T. Vogt, $A_2Cu_2CoO_2S_2$ (A = Sr, Ba), a novel example of a square-planar CoO_2 layer, J. Am. Chem. Soc. **119**, 12398 (1997).

[4] K. Otzschi, H. Ogino, J. Shimoyama, and K. Kishio, New candidates for superconductors; A series of layered oxysulfides $(Cu_2S_2)(Sr_{n+1}M_nO_{3-1})$, J. Low Temp. Phys. **117**, 729 (1999).

[5] R. Nath, V. O. Garlea, A. I. Goldman, and D. C. Johnston, Synthesis, structure, and properties of tetragonal $Sr_2M_3As_2O_2$ ($M3 = Mn_3$, Mn_2Cu, and $MnZn_2$) compounds containing alternating CuO_2-type and FeAs-type layers, Phys. Rev. B **81**, 224513 (2010).

[6] H. Zhang, S. F. Jin, L. W. Guo, S. J. Shen, Z. P. Lin, and X. L. Chen, Bandgap narrowing in the layered oxysulfide semiconductor $Ba_3Fe_2O_5Cu_2S_2$: Role of FeO_2 layer, Chin. Phys. B **25**, 026101 (2016).

[7] W. M. Li, Z. M. Fu, X. C. Wang, J. Zhang, M. Liu, J. F. Zhao, M. L. Jin, G. Q. Zhao, G. Y. Dai, Z. Deang, S. J. Zhang, S. M. Feng, Z. Hu, Q. Z. Huang, H. J. Lin, C. T. Chen, Y. F. Yang, and C. Q. Jin, Synthesis, structure, and properties of the layered oxyselenide $Ba_2CuO_2Cu_2Se_2$, Inorg. Chem. **57**, 5108 (2018).

[8] B. Arah, C. Ritter, G. B. G. Stenning, and A. C. Mclaughlin, Magnetic phase separation in the oxypnictide $Sr_2Cr_{1.85}Mn_{1.15}As_2O_2$, Inorg. Chem. **61**, 12518 (2022).

[9] J. G. Bednorz and K. A. Muller, Possible high TC superconductivity in the Ba−La−Cu−O system, Z. Phys. B Condens. Matter **64**, 189 (1986).

[10] M. K. Wu, J. R. Ashburn, C. J. Tong, P. H. Hor, R. L. Meng, L. Gao, Z. J. Huang, Y. Q. Wang, and C. W. Chu, Superconductivity at 93 K in a new mixed-phase Y-Ba-Cu-O compound system at ambient pressure, Phys. Rev. Lett. **58**, 908 (1987).

[11] A. Schilling, M. Cantoni, J. D. Guo, and H. R. Ott, Superconductivity above 130 k in the Hg–Ba–Ca–Cu–O system, Nature (London) **363**, 56 (1993).

[12] C. Q. Jin, X. J. Wu, P. Laffez, T. Tatsuki, T. Tamura, S. Adachi, H. Yamauchi, N. Koshizuka, and S. Tanaka, Superconductivity at 80 K in (Sr,Ca)3Cu2O4+δCl2-y induced by apical oxygen doping, Nature (London) **375**, 301 (1995).

[13] M. Horio, M. Miyamoto, Y. Mino, S. Ishida, B. Thiagarajan, C. M. Polley, C. H. Lee, T. Nishio, H. Eisaki, and I. Matsuda,

Enhanced superconducting gap in the outer CuO_2 plane of the trilayer cuprate (Hg, Re)$Ba_2Ca_2Cu_3O_{8+\delta}$, Phys. Rev. Lett. **135**, 046501 (2025).

[14] Y. Kamihara, T. Watanabe, M. Hirano, and H. Hosono, Iron-based layered superconductor La[$O_{1-x}F_x$]FeAs (x = 0.05 − 0.12) with T_c = 26 K, J. Am. Chem. Soc. **130**, 3296 (2008).

[15] M. Rotter, M. Tegel, and D. Johrendt, Superconductivity at 38 K in the Iron Arsenide ($Ba_{1-x}K_x$)Fe_2As_2, Phys. Rev. Lett. **101**, 107006 (2008).

[16] X. C. Wang, Q. Q. Liu, Y. X. Lv, W. B. Gao, L. X. Yang, R. C. Yu, F. Y. Li, and C. Q. Jin, The superconductivity at 18 K in LiFeAs system, Solid State Commun. **148**, 538 (2008).

[17] G. R. Stewart, Superconductivity in iron compounds, Rev. Mod. Phys. **83**, 1589 (2011).

[18] C. Dong, Q. Xu, and Y. Ma, Towards high-field applications: High-performance, low-cost iron-based superconductors, Nat. Sci. Rev. **11**, nwae122 (2024).

[19] J. N. Blandy, S. Liu, C. F. Smura, S. J. Cassidy, D. N. Woodruff, J. E. McGrady, and S. Clarke, Synthesis, structure, and properties of the layered oxide chalcogenides $Sr_2CuO_2Cu_2S_2$ and $Sr_2CuO_2Cu_2Se_2$, Inorg. Chem. **57**, 15379 (2018).

[20] T. L. Chou, O. Mustonen, T. S. Tripathi, and M. Karppinen, Isovalent Ca and Ba substitutions in thermoelectric layer-structured oxyselenide $Sr_2CoO_2Cu_2Se_2$, J. Phys.: Condens. Matter **28**, 035802 (2016).

[21] Y. Yang, Z. Zhou, B. Wei, J. Liu, J.-L. Lan, M. Zou, Y. Xu, Y. Zheng, C.-W. Nan, and Y.-H. Lin, Thermoelectric properties of layered oxyselenides with 3D transition metal ions, J. Am. Ceram. Soc. **106**, 2918 (2023).

[22] R. D. Smyth, J. N. Blandy, Z. Y. Yu, S. Liu, C. V. Topping, S. J. Cassidy, C. F. Smura, D. N. Woodruff, P. Manuel, C. L. Bull, N. P. Funnell, C. J. Ridley, J. E. McGrady, and S. J. Clarke, High- versus low-spin Ni^{2+} in elongated octahedral environments: $Sr_2NiO_2Cu_2Se_2$, $Sr_2NiO_2Cu_2S_2$, and $Sr_2NiO_2Cu_2(Se_{1-x}S_x)_2$, Chem. Mater. **34**, 9503 (2022).

[23] X. Cheng, Z. Zhang, Q. Kong, Q. H. Zhang, T. Wang, S. M. Dong, L. Gu, X. Wang, J. Ma, P. X. Han, H. J. Lin, C. T. Chen, and G. L. Cui, Highly reversible cuprous mediated cathode chemistry for magnesium batteries, Angew. Chem. Int. Ed. **59**, 11477 (2020).

[24] D. F. Li, K. Lee, B. Y. Wang, M. Osada, S. Crossley, H. R. Lee, Y. Cui, Y. Hikita, and H. Y. Hwang, Superconductivity in an infinite-layer nickelate, Nature (London) **572**, 624 (2019).

[25] S. W. Zeng, C. S. Tang, X. M. Yin, C. J. Li, M. S. Li, Z. Huang, J. X. Hu, W. Liu, G. J. Omar, H. Jani, Z. S. Lim, K. Han, D. Y. Wan, P. Yang, S. J. Pennycook, A. T. S. Wee, and A. Ariando, Phase diagram and superconducting dome of infinite-layer $Nd_{1-x}Sr_xNiO_2$ thin films, Phys. Rev. Lett. **125**, 147003 (2020).

[26] M. Hirayama, T. Tadano, Y. Nomura, and R. Arita, Materials design of dynamically stable d^9 layered nickelates, Phys. Rev. B **101**, 075107 (2020).

[27] H. Sakakibara, H. Usui, K. Suzuki, T. Kotani, H. Aoki, and K. Kuroki, Model construction and a possibility of cupratelike pairing in a new d^9 Nickelate Superconductor (Nd,Sr)NiO_2, Phys. Rev. Lett. **125**, 077003 (2020).

[28] Y. X. Wang, K. Jiang, J. J. Ying, T. Wu, J. G. Cheng, J. P. Hu, and X. H. Chen, Recent progress in nickelate superconductors, Nat. Sci. Rev. **12**, nwaf373 (2025).

[29] H. L. Sun, M. W. Huo, X. W. Hu, J. Y. Li, Y. F. Han, L. Y. Tang, Z. Q. Mao, P. T. Yang, B. S. Wang, J. G. Cheng, D. X. Yao, G. M. Zhang, and M. Wang, Signatures of superconductivity near 80 K in a nickelate under high pressure, Nature (London) **621**, 493 (2023).

[30] Y. H. Zhu, D. Peng, E. K. Zhang, B. Y. Pan, X. Chen, L. X. Chen, H. F. Ren, F. Y. Liu, Y. Q. Hao, N. N. Li, Z. F. Xing, F. J. Lan, J. Y. Han, J. J. Wang, D. H. Jia, H. L. Wo, Y. Q. Gu, Y. M. Gu, L. Ji, *et al.*, Superconductivity in pressurized trilayer $La_4Ni_3O_{10-\delta}$ single crystals, Nature (London) **631**, 531 (2024).

[31] M. H. Shi, D. Peng, K. B. Fan, Z. F. Xing, S. H. Yang, Y. Z. Wang, H. P. Li, R. Q. Wu, M. Du, B. H. Ge, Z. D. Zeng, Q. S. Zeng, J. J. Ying, T. Wu, and X. H. Chen, Pressure induced superconductivity in hybrid Ruddlesden-Popper $La_5Ni_3O_{11}$ single crystals, Nat. Phys. **21**, 1780 (2025).

[32] S. J. Clarke, P. Adamson, S. J. C. Herkelrath, O. J. Rutt, D. R. Parker, M. J. Pitcher, and C. F. Smura, Structures, physical properties, and chemistry of layered oxychalcogenides and oxypnictides, Inorg. Chem. **47**, 8473 (2008).

[33] Y. Matsumoto, T. Yamamoto, K. Nakano, H. Takatsu, T. Murakami, K. Hongo, R. Maezono, H. Ogino, D. Song, C. M. Brown, C. Tassel, and H. Kageyama, High-pressure synthesis of $A_2NiO_2Ag_2Se_2$ (A = Sr, Ba) with a high-spin Ni^{2+} in square-planar coordination, Angew. Chem. Int. Ed. **58**, 756 (2019).

[34] R. R. P. Singh, Magnetism of competing high-spin/low-spin states in $Ba_2NiO_2(AgSe)_2$ and related two-orbital two-electron systems, Phys. Rev. B **105**, 064406 (2022).

[35] R. C. Liebermann, Multi-anvil, high pressure apparatus: A half-century of development and progress, High Pressure Res. **31**, 493 (2011).

[36] X. Ye, X. Wang, Z. Liu, B. Zhou, L. Zhou, H. Deng, and Y. Long, Emergent physical properties of perovskite-type oxides prepared under high pressure, Dalton Trans. **51**, 1745 (2022).

[37] M. Du and D. He, Gas encapsulation technology for large volume press, Chin. Phys. B **33**, 110701 (2024).

[38] X. Wang, X. Ye, Z. Liu, and Y. Long, High-pressure synthesis and research progress of multi-order perovskite oxides, Chin. Sci. Bull. **70**, 3470 (2025).

[39] H. M. Rietveld, A profile refinement method for nuclear and magnetic structures, J. Appl. Crystallogr. **2**, 65 (1969).

[40] R. Von Dreele, Quantitative texture analysis by Rietveld refinement, J. Appl. Crystallogr. **30**, 517 (1997).

[41] W. Liu, J. Feng, W. Zhou, S. Li, and Z. Shi, High-pressure studies on quasi-one-dimensional systems, Chin. Phys. B **34**, 088104 (2025).

[42] C. T. Chantler, G. Bunker, P. D'angelo, and S. Diaz-Moreno, X-ray absorption spectroscopy, Nat. Rev. Methods Primers **4**, 89 (2024).

[43] B. H. Frazer, B. Gilbert, B. R. Sonderegger, and G. De Stasio, The probing depth of total electron yield in the sub-keV range: TEY-XAS and X-PEEM, Surf. Sci. **537**, 161 (2003).

[44] R. M. Trevorah, C. T. Chantler, and M. J. Schalken, Solving self-absorption in fluorescence, IUCrJ **6**, 586 (2019).

[45] P. Blaha, K. Schwarz, F. Tran, R. Laskowski, G. K. H. Madsen, and L. D. Marks, WIEN2k: An APW+lo program for calculating the properties of solids, J. Chem. Phys. **152**, 074101 (2020).

[46] J. P. Perdew, K. Burke, and M. Ernzerhof, Generalized gradient approximation made simple, Phys. Rev. Lett. **77**, 3865 (1996).

[47] Y. Cao and Y. Yang, Flat bands promoted by Hund's rule coupling in the candidate double-layer high-temperature superconductor $La_3Ni_2O_7$ under high pressure, Phys. Rev. B **109**, L081105 (2024).

[48] X. Wan, V. Ivanov, G. Resta, I. Leonov, and S. Y. Savrasov, Exchange interactions and sensitivity of the Ni two-hole spin state to Hund's coupling in doped $NdNiO_2$, Phys. Rev. B **103**, 075123 (2021).

[49] I. D. Brown and D. Altermatt, Bond-valence parameters obtained from a systematic analysis of the inorganic crystal structure database, Acta. Cryst. B **41**, 244 (1985).

[50] N. E. Brese and M. O'Keeffe, Bond-valence parameters for solids, Acta. Cryst. B **47**, 192 (1991).

[51] X. B. Ye, Y. Y. Yin, Y. Y. Cao, Z. Y. Liao, X. Wang, M. Liu, Q. Q. Wang, Z. Pan, Z. Hu, H. J. Lin, C. T. Chen, C. W. Pao, P. Ohresser, L. Nataf, F. Baudelet, W. Y. Yang, J. B. Yang, J. G. Cheng, P. Yu, *et al.*, High-temperature ferrimagnetic order triggered metal-to-insulator transition in $CaCu_3Ni_2Os_2O_{12}$, Nat. Commun. **16**, 3746 (2025).

[52] M. C. Pi, J. Y. Yang, J. Zhang, X. B. Ye, X. Wang, L. H. He, Z. Hu, C. T. Chen, C. Y. Kuo, Z. Pan, Y. Shen, and Y. W. Long, Observation of robust compressed CuO_6 octahedra and exotic spin structure in $CaCuFe_2O_5$, J. Am. Chem. Soc. **147**, 4403 (2025).

[53] X. Wang, Z. Hu, S. Agrestini, J. Herrero-Martin, M. Valvidares, R. Sankar, F.-C. Chou, Y.-H. Chu, A. Tanaka, L. H. Tjeng, and E. Pellegrin, Evidence for largest room temperature magnetic signal from Co^{2+} in antiphase-free & fully inverted $CoFe_2O_4$ in multiferroic-ferrimagnetic $BiFeO_3$-$CoFe_2O_4$ nanopillar thin films, J. Magn. Magn. Mater. **530**, 167940 (2021).

[54] L. H. Tjeng, C. T. Chen, and S.-W. Cheong, Comparative soft-x-ray resonant-photoemission study on $Bi_2Sr_2CaCu_2O_8$, CuO, and Cu_2O, Phys. Rev. B **45**, 8205(R) (1992).

[55] Z. Hu, S.-L. Drechsler, J. Malek, H. Rosner, R. Neudert, M. Knupfer, M. S. Golden, J. Fink, J. Karpinski, G. Kaindl, C. Hellwig, and Ch. Jung, Doped holes in edge-shared CuO_2 chains and the dynamic spectral weight transfer in X-ray absorption spectroscopy, Europhys. Lett. **59**, 135 (2002).

[56] M. Grioni, J. B. Goedkoop, R. Schoorl, F. M. F. de Groot, J. C. Fuggle, F. Schäfers, E. E. Koch, G. Rossi, J.-M. Esteva, and R. C. Karnatak, Doped holes in edge-shared CuO_2 chains and the dynamic spectral weight transfer in X-ray absorption spectroscopy, Phys. Rev. B **39**, 1541 (1989).

[57] X. Wang, F. Temnikov, X. B. Ye, M. C. Pi, Z. Pan, W. H. Li, Z. Hu, C. T. Chen, C. Y. Kuo, C. Dong, Y. Shen, W. M. Li, S. V. Streltsov, and Y. W. Long, $CuCu_3Fe_2Os_2O_{12}$: A room-temperature ferrimagnet with reduced thermal conductivity, Inorg. Chem. **64**, 20796 (2025).

[58] M. Abbate, G. Zampieri, F. Prado, A. Caneiro, J. M. Gonzalez-Calbet, and M. Vallet-Regi, Electronic structure and metal-insulator transition in $LaNiO3_{-\delta}$, Phys. Rev. B **65**, 155101 (2002).

[59] S. L. Brock, N. P. Raju, J. E. Greedan, and S. M. Kauzlarich, The magnetic structures of the mixed layer pnictide oxide compounds $Sr_2Mn_3Pn_2O_2$ (Pn = As, Sb), J. Alloys Compd. **237**, 9 (1996).

[60] K. Binder and A. P. Young, Spin glasses: Experimental facts, theoretical concepts, and open questions, Rev. Mod. Phys. **58**, 801 (1986).

[61] S. Mahana and D. Topwal, Complex spin glass behavior in $Ga_{2-x}Fe_xO_3$, Appl. Phys. Lett. **110**, 102907 (2017).

[62] P. N. Lekshimi, G. R. Raji, M. Vasundhara, M. R. Varma, S. S. Pillai, and M. Valant, Re-entrant spin glass behaviour and magneto-dielectric effect in insulating Sm_2NiMnO_6 double perovskite, J. Mater. Chem. C **1**, 6565 (2013).

[63] J. Zhang, L. Duan, Z. Wang, X. Wang, J. Zhao, M. Jin, W. Li, C. Zhang, L. Cao, Z. Deng, Z. Hu, S. Agrestini, M. Valvidares, H.-J. Lin, C.-T. Chen, J. Zhu, and C. Jin, The synthesis of a quasi-one-dimensional iron-based telluride with antiferromagnetic chains and a spin glass state, Inorg. Chem. **59**, 5377 (2020).

[64] C. F. Smura, D. R. Parker, M. Zbiri, M. R. Johnson, Z. A. Gal, and S. J. Clarke, High-spin cobalt(II) ions in square planar coordination: Structures and magnetism of the oxysulfides $Sr_2CoO_2Cu_2S_2$ and $Ba_2CoO_2Cu_2S_2$ and their solid solution, J. Am. Chem. Soc. **133**, 2691 (2011).

[65] S. Jin, X. Chen, J. Guo, M. Lei, J. Lin, J. Xi, W. Wang, and W. Wang, $Sr_2Mn_3Sb_2O_2$ type oxyselenides: Structures, magnetism, and electronic properties of $Sr_2AO_2M_2Se_2$ (A = Co, Mn; M = Cu, Ag), Inorg. Chem. **51**, 10185 (2012).

[66] W. M. Li, J. F. Zhao, L. P. Cao, Z. Hu, Q. Z. Huang, X. C. Wang, Y. Liu, G. Q. Zhao, J. Zhang, Q. Q. Liu, R. Z. Yu, Y. W. Long, H. Wu, H. J. Lin, C. T. Chen, Z. Li, Z. Z. Gong, Z. Guguchia, J. S. Kim, *et al.*, Superconductivity in a unique type of copper oxide, Proc. Natl Acad. Sci. USA **116**, 12156 (2019).

[67] K. Jiang, C. C. Le, Y. X. Li, S. S. Qin, Z. Q. Wang, F. C. Zhang, and J. P. Hu, Electronic structure and two-band superconductivity in unconventional high-T_c cuprates $Ba_2CuO_{3+\delta}$, Phys. Rev. B **103**, 045108 (2021).

[68] F. Birch, Finite elastic strain of cubic crystals, Phys. Rev. **71**, 809 (1947).

[69] https://lssf.cas.cn/sszs/ggsy/shgy/.